Applied Mathematical Modelling 44 (2017) 409–424

Contents lists available at ScienceDirect

Applied Mathematical Modelling

journal homepage: www.elsevier.com/locate/apm

Verification and validation of the foredrag coefficient for supersonic and hypersonic flow of air over a cone of fineness ratio 3

Guilherme Bertoldo [a,b,*], Carlos Henrique Marchi [a]

[a] Laboratory of Numerical Experimentation (LENA), Department of Mechanical Engineering (DEMEC), Universidade Federal do Paraná (UFPR), Caixa postal 19040, Zip Code 81531-980, Curitiba, Paraná, Brazil

[b] On temporary leave from Department of Physics, Statistics and Mathematics (DAFEM), Universidade Tecnológica Federal do Paraná (UTFPR), Campus Francisco Beltrão, Zip Code 85601-970, Francisco Beltrão, Paraná, Brazil

ARTICLE INFO

Article history:
Received 12 December 2015
Revised 20 January 2017
Accepted 30 January 2017
Available online 10 February 2017

Keywords:
CFD
Verification
Validation
Cone
Supersonic
Hypersonic

ABSTRACT

The foredrag coefficient resulting from the supersonic and hypersonic flow of air over a cone was calculated numerically using a finite volume approach based on the compressible Euler and Navier-Stokes equations with constant and variable thermophysical properties. No turbulence model was considered. Simulations were carried out for a cone of fineness ratio 3 under the free-stream Mach numbers 2.73, 3.50, 4.00, 5.05 and 6.28 (the Reynolds number, based on cone length, is within 0.45 and 2.85 million). Up to six grids were employed for numerical calculations, with 60 × 60 to 1920 × 1920 volumes. The numerical error was estimated to be less than 0.01% of the numerical solution for all models. Comparisons of the numerical foredrag coefficients of the three models with the experimental data showed that the Navier–Stokes model with variable thermophysical properties agreed better with the experimental foredrag for the entire Mach number interval studied, taking into account the validation standard uncertainty.

1. Introduction

Increased computer power in the past decades has led to a widespread use of numerical methods to solve fluid dynamics problems, followed by an increased interest of the scientific community on the accuracy and reliability of numerical solutions. There are several papers (see, for instance, Ref. [1-4]) and entire books [5–7] addressing this issue.

According to Roache [7], the estimation/quantification of errors/uncertainties in Computational Fluid Dynamics (CFD) are performed through verification and validation. Verification estimates/quantifies the error/uncertainty caused by solving approximately a mathematical model, while validation estimates/quantifies the error/uncertainty caused by the modeling itself. Verification can be divided into code verification and solution verification. Code verification aims to eliminate or, at least, minimize the chance of coding mistakes (bugs), while solution verification aims to estimate/quantify the numerical errors/uncertainties related to the approximations applied to solve the mathematical model.

* Corresponding author at: Department of Physics, Statistics and Mathematics (DAFEM), Universidade Tecnológica Federal do Paraná (UTFPR), Campus Francisco Beltrão, Zip Code 85601-970, Francisco Beltrão, Paraná, Brazil

E-mail addresses: gbertoldo@utfpr.edu.br, glbertoldo@gmail.com (G. Bertoldo), machi@pq.cnpq.br (C.H. Marchi).

http://dx.doi.org/10.1016/j.apm.2017.01.090
0307-904X/

Despite the above mentioned progress in CFD and error quantification, based on the authors' experience, verified and tabulated numerical solutions for the flow over basic geometries, such as the conical one, are still not widely found in the open literature. This type of data is especially useful when comparing mathematical models or checking the results of a new software in its early development stage, for instance.

Accordingly, the aim of this work is to numerically determine the foredrag coefficient of the classical conical flow problem [8] and its numerical uncertainty for three mathematical models: (i) Euler equations, (ii) Navier–Stokes equations with constant thermophysical properties (NS-C) and (iii) Navier–Stokes equations with variable thermophysical properties (NS-V). No turbulence model is considered. Additionally, this work aims to estimate the modeling error, and associated uncertainty, of the investigated models by comparing the numerical solutions with the experimental data of Eggers et al. [9].

The calculations are limited to a cone of fineness ratio $f = 3$ (length/base diameter) and to the free-stream Mach numbers 2.73, 3.50, 4.00, 5.05 and 6.28[1]. The free-stream Reynolds number, based on the cone length, vary from 4.5×10^5 to 2.85×10^6. The cone geometry was chosen because the solutions of the Taylor–Maccoll equation [11] (a specialization of the Euler equations for the conical flow) can be obtained so accurately with nowadays computers, that they can be treated as analytical. Moreover, the Mach numbers, Reynolds number and cone aspect ratio were chosen because of the available experimental data of Eggers et al. [9], which are used in the validation.

Verification and validation procedures are applied here based on the recommendations of ASME V&V 20–2009 Standard [12]. During this process, the convergent estimator [13,14] is applied to obtain higher order solutions from the numerical one and some difficulties related to the validation are exposed.

2. Methodology

2.1. Flow simulation

Flow is modeled by the time dependent, axisymmetric, compressible Euler and Navier–Stokes equations [15]. The Euler model is obtained from the Navier–Stokes one by neglecting all terms depending on the viscosity and thermal conductivity. This work focuses on the steady state solution. Time dependence is applied to make the solution algorithm stable.

The thermophysical properties, *i.e.*, viscosity μ, thermal conductivity κ and specific heats at constant pressure c_p and volume c_v, may be considered constant and equal to their free-stream values or they may be functions of the local temperature T. In this study, the fluid (air) is a mixture of Ar, O_2 and N_2 in the mole fractions of $X_1 = 1\%$, $X_2 = 21\%$ and $X_3 = 78\%$, respectively. In order to calculate c_p, μ and κ of the gas mixture, the corresponding thermophysical properties $(c_p)_i$, μ_i and κ_i of each chemical specie i are first calculated according to the interpolation formulas of McBride et al. [16] as

$$(c_p)_i = (R_g)_i\left[A_i + B_i T + C_i T^2 + D_i T^3 + E_i T^4\right], \tag{1}$$

$$\mu_i = \exp\left(A_i' \ln\left(\frac{T}{\mathrm{K}}\right) + \frac{B_i'}{T} + \frac{C_i'}{T^2} + D_i'\right) \cdot 10^{-7} \text{ Pa s}, \tag{2}$$

and

$$\kappa_i = \exp\left(A_i'' \ln\left(\frac{T}{\mathrm{K}}\right) + \frac{B_i''}{T} + \frac{C_i''}{T^2} + D_i''\right) \cdot 10^{-4} \text{ W m}^{-1}\text{K}^{-1}, \tag{3}$$

where the gas constant of each specie $(R_g)_i$ and the coefficients A_i to D_i'' are given by McBride et al.

The thermophysical properties for the gas mixture are calculated according to Refs. [15] and [17] as

$$c_p = \sum_{i=1}^{3} X_i M_i (c_p)_i \Big/ \sum_{i=1}^{3} X_i M_i, \tag{4}$$

$$\mu = \sum_{i=1}^{3} \frac{X_i \mu_i}{\sum_{j=1}^{3} X_j \Phi_{ij}^{\mu}}, \tag{5}$$

$$\kappa = \sum_{i=1}^{3} \frac{X_i \kappa_i}{\sum_{j=1}^{3} X_j \Phi_{ij}^{\kappa}}, \tag{6}$$

where

$$\Phi_{ij}^{\psi} = \frac{1}{\sqrt{8}}\left(1 + \frac{M_i}{M_j}\right)^{-1/2}\left[1 + \left(\frac{\psi_i}{\psi_j}\right)^{1/2}\left(\frac{M_j}{M_i}\right)^{1/4}\right]^2, \quad \psi \in \{\mu, \kappa\} \tag{7}$$

[1] Some preliminary results were presented in CMAC-SE conference [10].

and M_i is the molecular mass of chemical specie i.

The ideal gas state equation is used for the coupling among pressure p, density ρ and temperature T, *i.e.*,

$$p = \rho R_g T, \tag{8}$$

where R_g is the gas constant.

In order to simplify the procedure of obtaining the numerical solution, the governing equations are transformed [18] from the cylindrical coordinate system (x, r) to a curvilinear coordinate system (ξ, η), in such a way that the physical domain is mapped into a rectangular domain (computational domain). These equations are summarized as follow

$$\begin{aligned} C^\phi\left[\frac{1}{J}\frac{\partial(\rho\phi)}{\partial t}+\frac{1}{r}\frac{\partial(\rho r U\phi)}{\partial\xi}+\frac{1}{r}\frac{\partial(\rho r V\phi)}{\partial\eta}\right] &= \frac{1}{r}\frac{\partial}{\partial\xi}\left[\Gamma^\phi rJ\left(\hat{\alpha}\frac{\partial\phi}{\partial\xi}-\hat{\beta}\frac{\partial\phi}{\partial\eta}\right)\right] \\ &+\frac{1}{r}\frac{\partial}{\partial\eta}\left[\Gamma^\phi rJ\left(\hat{\gamma}\frac{\partial\phi}{\partial\eta}-\hat{\beta}\frac{\partial\phi}{\partial\xi}\right)\right] \\ &+P^\phi+S^\phi, \end{aligned} \tag{9}$$

where ϕ is a generic variable that represents 1, u, v or T, u and v are the components of the velocity vector $\boldsymbol{u}$ in the directions of x and r, respectively, and t is the time. Depending on the choice of ϕ, Eq. (9) represents: the mass conservation equation ($\phi = 1$), the momentum conservation equation in the x direction ($\phi = u$), the momentum conservation equation in the r direction ($\phi = v$) or the thermal energy conservation equation ($\phi = T$). The remaining symbols of Eq. (9) are U and V, the contravariant components of the velocity vector,

$$U = ur_\eta - vx_\eta, \qquad V = vx_\xi - ur_\xi, \tag{10}$$

the Jacobian of the coordinate transformation J,

$$J = \left[x_\xi r_\eta - x_\eta r_\xi\right]^{-1}, \tag{11}$$

the components of the metric tensor $\hat{\alpha}$, $\hat{\beta}$ and $\hat{\gamma}$,

$$\hat{\alpha} = x_\eta^2 + r_\eta^2, \qquad \hat{\beta} = x_\xi x_\eta + r_\xi r_\eta, \qquad \hat{\gamma} = x_\xi^2 + r_\xi^2, \tag{12}$$

where the sub-indexes ξ and η mean partial derivatives, *i.e.*,

$$x_\xi = \frac{\partial x}{\partial\xi}, \quad x_\eta = \frac{\partial x}{\partial\eta}, \quad r_\xi = \frac{\partial r}{\partial\xi}, \quad r_\eta = \frac{\partial r}{\partial\eta}. \tag{13}$$

The symbols C^ϕ, Γ^ϕ and P^ϕ are given in Table 1, while S^ϕ is presented in Table 1 or in Eqs. (14)–(16):

$$\begin{aligned} S^u = &\frac{1}{3}\frac{\partial}{\partial\xi}\left[J\mu\left(r_\eta^2\frac{\partial u}{\partial\xi}-r_\xi r_\eta\frac{\partial u}{\partial\eta}\right)\right]+\frac{1}{3}\frac{\partial}{\partial\eta}\left[J\mu\left(r_\xi^2\frac{\partial u}{\partial\eta}-r_\xi r_\eta\frac{\partial u}{\partial\xi}\right)\right] \\ &+\frac{1}{r}\frac{\partial}{\partial\xi}\left[Jr\mu x_\eta\left(r_\xi\frac{\partial v}{\partial\eta}-r_\eta\frac{\partial v}{\partial\xi}\right)\right]+\frac{1}{r}\frac{\partial}{\partial\eta}\left[Jr\mu x_\xi\left(r_\eta\frac{\partial v}{\partial\xi}-r_\xi\frac{\partial v}{\partial\eta}\right)\right] \\ &-\frac{2}{3}\frac{\partial}{\partial\xi}\left[J\frac{\mu}{r}r_\eta\left(x_\xi\frac{\partial(rv)}{\partial\eta}-x_\eta\frac{\partial(rv)}{\partial\xi}\right)\right] \\ &-\frac{2}{3}\frac{\partial}{\partial\eta}\left[J\frac{\mu}{r}r_\xi\left(x_\eta\frac{\partial(rv)}{\partial\xi}-x_\xi\frac{\partial(rv)}{\partial\eta}\right)\right], \end{aligned} \tag{14}$$

$$\begin{aligned} S^v = &\frac{1}{3r}\frac{\partial}{\partial\xi}\left[J\mu r\left(x_\eta^2\frac{\partial v}{\partial\xi}-x_\xi x_\eta\frac{\partial v}{\partial\eta}\right)\right]+\frac{1}{3r}\frac{\partial}{\partial\eta}\left[J\mu r\left(x_\xi^2\frac{\partial v}{\partial\eta}-x_\xi x_\eta\frac{\partial v}{\partial\xi}\right)\right] \\ &+\frac{\partial}{\partial\xi}\left[J\mu r_\eta\left(x_\xi\frac{\partial u}{\partial\eta}-x_\eta\frac{\partial u}{\partial\xi}\right)\right]+\frac{\partial}{\partial\eta}\left[J\mu r_\xi\left(x_\eta\frac{\partial u}{\partial\xi}-x_\xi\frac{\partial u}{\partial\eta}\right)\right] \end{aligned}$$

Table 1
Symbols C^ϕ, Γ^ϕ, P^ϕ and S^ϕ of Eq. (9).

ϕ	C^ϕ	Γ^ϕ	P^ϕ	S^ϕ
1	1	0	0	0
u	1	μ	$\frac{\partial(pr_\xi)}{\partial\eta}-\frac{\partial(pr_\eta)}{\partial\xi}$	Eq. (14)
v	1	μ	$\frac{\partial(px_\eta)}{\partial\xi}-\frac{\partial(px_\xi)}{\partial\eta}$	Eq. (15)
T	c_p	κ	$\frac{1}{J}\frac{\partial p}{\partial t}$	Eq. (16)

$$-\frac{2}{3}\frac{\partial}{\partial\xi}\left[J\mu x_\eta\left(r_\xi\frac{\partial u}{\partial\eta}-r_\eta\frac{\partial u}{\partial\xi}\right)\right]-\frac{2}{3}\frac{\partial}{\partial\eta}\left[J\mu x_\xi\left(r_\eta\frac{\partial u}{\partial\xi}-r_\xi\frac{\partial u}{\partial\eta}\right)\right]$$
$$-\frac{4}{3}\frac{\mu v}{r^2 J}-\frac{2v}{3r}\left[\frac{\partial}{\partial\eta}\left(x_\xi\mu\right)-\frac{\partial}{\partial\xi}\left(x_\eta\mu\right)\right], \tag{15}$$

$$S^T=-\frac{1}{r}\left[\frac{1}{J}\frac{\partial(\rho rK)}{\partial t}+\frac{\partial(\rho rUK)}{\partial\xi}+\frac{\partial(\rho rVK)}{\partial\eta}\right]$$
$$+\frac{1}{r}\frac{\partial}{\partial\xi}\left\{r\left[(v\sigma_{xr}+u\sigma_{xx})r_\eta-(v\sigma_{rr}+u\sigma_{xr})x_\eta\right]\right\}$$
$$+\frac{1}{r}\frac{\partial}{\partial\eta}\left\{r\left[(v\sigma_{rr}+u\sigma_{xr})x_\xi-(v\sigma_{xr}+u\sigma_{xx})r_\xi\right]\right\}, \tag{16}$$

where

$$K=\frac{u^2+v^2}{2}, \tag{17}$$

σ_{xx}, σ_{xr} and σ_{rr} are the components of the viscous stress tensor, *i.e.*,

$$\sigma_{xx}=2\mu\frac{\partial u}{\partial x}-\frac{2}{3}\mu\nabla\cdot\boldsymbol{u}, \tag{18}$$

$$\sigma_{rr}=2\mu\frac{\partial v}{\partial r}-\frac{2}{3}\mu\nabla\cdot\boldsymbol{u}, \tag{19}$$

$$\sigma_{xr}=\mu\left(\frac{\partial v}{\partial x}+\frac{\partial u}{\partial r}\right) \tag{20}$$

and

$$\nabla\cdot\boldsymbol{u}=\frac{\partial u}{\partial x}+\frac{\partial v}{\partial r}+\frac{v}{r}. \tag{21}$$

The derivatives of u and v with respect to x and r are given by

$$\frac{\partial\phi}{\partial x}=J\left(r_\eta\frac{\partial\phi}{\partial\xi}-r_\xi\frac{\partial\phi}{\partial\eta}\right),\qquad \phi\in\{u,v\} \tag{22}$$

and

$$\frac{\partial\phi}{\partial r}=J\left(x_\xi\frac{\partial\phi}{\partial\eta}-x_\eta\frac{\partial\phi}{\partial\xi}\right),\qquad \phi\in\{u,v\}. \tag{23}$$

In the case of inviscid flow with constant thermophysical properties, the stationary temperature field T is obtained from the conservation of total enthalpy:

$$T=\frac{1}{(c_p)_\infty}\left[(c_p)_\infty T_\infty+\frac{u_\infty^2-u^2-v^2}{2}\right], \tag{24}$$

where the index ∞ means the free-stream value of the variable.

The quantity of interest is the foredrag coefficient C_{Df}, given by

$$C_{\mathrm{Df}}=\frac{2}{q_\infty r_b^2}\int_{\xi_i}^{\xi_f}\left[(p-p_\infty)r_\xi+\sigma_{xr}x_\xi-\sigma_{xx}r_\xi\right]r\,\mathrm{d}\xi, \tag{25}$$

where r_b is the cone base radius, ξ_i and ξ_f are the initial and final values of ξ along the cone surface.

The domain of calculation, Fig 1a, is simplified due to the axial symmetry. Over the north boundary N (a quarter of ellipse), the flow is non-perturbed and equal to the free-stream, where the Mach number M_∞, Reynolds number Re_∞ (based on the cone length l_r) and temperature T_∞ are prescribed. On the west boundary W, the symmetry conditions are applied. Over the south boundary S, the normal pressure and temperature gradient are zero, while the non-slip condition, $u=v=0$, is applied to the velocity field in the case of the Navier–Stokes model and the slip condition, $\hat{n}\cdot\boldsymbol{u}=0$, is applied to the Euler model, where $\hat{n}$ is the unitary vector normal to the body surface. Finally, the variables $\phi\in\{u, v, T, p\}$ on the east boundary E (outflow) are approximated with

$$\frac{\partial\phi}{\partial\xi}=0, \tag{26}$$

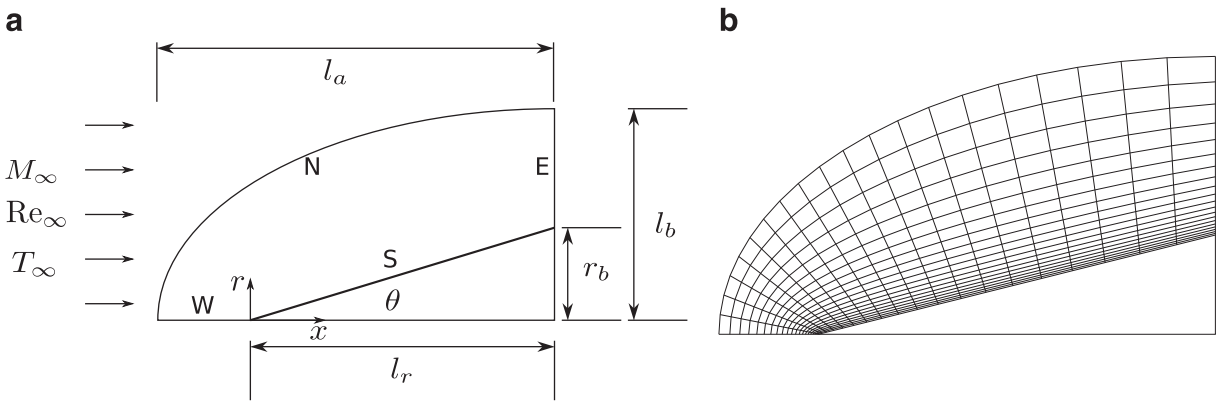

Fig. 1. Schematic illustration of the (a) domain of calculation and (b) its discretization.

for the Navier–Stokes model and with

$$\boldsymbol{r}\cdot\nabla\phi = 0 \Rightarrow \left(xr_\eta - rx_\eta\right)\frac{\partial\phi}{\partial\xi} + \left(rx_\xi - xr_\xi\right)\frac{\partial\phi}{\partial\eta} = 0, \tag{27}$$

for the Euler model, where $\boldsymbol{r}$ is the position vector. Eq. (27) provides an outflow boundary condition consistent with the Taylor–Maccoll equation.

The physical domain is algebraically discretized with nodes concentrated near the cone surface and the cone tip (Fig. 1b). The x coordinate of the south and north boundaries (η lines) is discretized according to a power law distribution with exponent α. The lines connecting the north and south boundaries (ξ lines) are discretized in such a way that the partition widths form a geometric progression. The width of the partition close to the cone surface is a multiple c_{bl} of the estimated boundary layer width δ, which is given by

$$\delta = \sqrt{\frac{\mu_\infty l_r}{\rho_\infty u_\infty}}, \tag{28}$$

where μ_∞, ρ_∞ and u_∞ are, respectively, the free-stream viscosity, density and speed. The transformed Navier–Stokes equations are then integrated on each volume of the uniformly discretized computational domain using a co-located grid arrangement. The variables over the volumes' faces are interpolated from the center of each volume in the computational domain using a first order accurate scheme (upstream differencing scheme) for the advective terms and a second order accurate scheme (central differencing scheme) for the diffusive terms [19]. Time derivatives are approximated with the fully implicit scheme (first order backward scheme)[19]. After that, four systems of coupled linearized equations are obtained representing the mass, momentum (x and r components) and thermal energy conservation. The discretized mass equation is transformed into an equation for the pressure correction based on the SIMPLEC algorithm [20]. The pressure correction equation takes into account the effects of compressibility as well as pressure-velocity coupling, in agreement with Ferziger and Peric [21]. For initial conditions, all fields are set to their corresponding free-stream values. At each instant of the discretized time line, the coupled linear systems, whose dependent variables are pressure deviation, the components of the velocity vector (u, v) and temperature T, are solved sequentially [21] (segregated approach) and iteratively with the *Modified Strongly Implicit* method (MSI) [22]. At this step, the iteration error is not reduced to the machine error, because the transient solution is not the focus here. Thus, a "false transient" is followed until a stationary solution is reached, within the machine error precision.

2.2. Verification

2.2.1. Code verification

The correctness of the code implementation will be evaluated through the Method of Manufactured Solutions (MMS) [7]. According to it, a solution is proposed and the differential equation and boundary conditions are adjusted through the addition of source terms, in such a way that the modified equations and boundary conditions satisfy the proposed solution.

Since MMS provides an analytical solution Φ, it is possible to evaluate the numerical error E and the order of convergence of the numerical solution p_E in a grid convergence study. The error E_i of a numerical solution ϕ_i is defined by

$$E_i = \phi_i - \Phi \tag{29}$$

and the order of convergence is given by

$$p_E = \log\left(\frac{\phi_2 - \Phi}{\phi_1 - \Phi}\right) \Big/ \log\left(\frac{h_2}{h_1}\right), \tag{30}$$

Table 2
Parameters of the manufactured solution.

Par.	Value	Par.	Value
a_x	2 m	ρ_∞ ($\lambda = 1$)	1 kg/m^3
a_r	1 m	ρ_∞ ($\lambda = 0$)	2.6727783×10^{-7} kg/m^3
φ_i	π	T_∞	300 K
φ_f	$\pi/2$	R_g	2.8700669×10^2 J/kg· K
ϱ_i	0.5 m	$(c_p)_\infty$	1.0044040×10^3 J/kg· K
ϱ_f	2 m	μ_∞	1.8559827×10^{-5} Pa· s
A	0.1	κ_∞	2.5730324×10^{-2} W/m· K
L	8 m	u_∞	6.9440203×10^2 m/s

where ϕ_1 and ϕ_2 are numerical solutions obtained in grids with partitions h_1 and h_2 ($h_2/h_1 > 1$), respectively.

In the manufactured solution of this work, the physical domain (x, r) and computational domain (ξ, η) are related through

$$x = a_x \varrho \cos(\varphi), \quad r = a_r \varrho \sin(\varphi) \tag{31}$$

and

$$\varphi = \varphi_i + (\varphi_f - \varphi_i)\frac{\xi}{N}, \quad \varrho = \varrho_i + (\varrho_f - \varrho_i)\frac{\eta}{N}, \qquad 0 \le \xi, \eta \le N, \tag{32}$$

where the parameters a_x, a_r, φ_i, φ_f, ϱ_i, ϱ_f are given in Table 2 and N means the number of volumes in each coordinate direction.

The manufactured solutions for ρ, T, c_p, μ, κ, u and v are given bellow:

$$\rho(x,r) = \rho_\infty\left[1 + \frac{A}{2}\left(\sin\left(\frac{2\pi}{L}x\right) + \cos\left(\frac{2\pi}{L}r\right)\right)\right], \tag{33}$$

$$T(x,r) = T_\infty\left\{1 + \lambda\frac{u_\infty^2 - u^2 - v^2}{2(c_p)_\infty T_\infty} + (1-\lambda)\frac{A}{2}\left[\sin\left(\frac{2\pi}{L}x\right) + \cos\left(\frac{2\pi}{L}r\right)\right]\right\}, \tag{34}$$

$$c_p(x,r) = (c_p)_\infty\left(\frac{T(x,r)}{T_\infty}\right)^m, \tag{35}$$

$$\mu(x,r) = \mu_\infty\left(\frac{T(x,r)}{T_\infty}\right)^m(1-\lambda), \tag{36}$$

$$\kappa(x,r) = \kappa_\infty\left(\frac{T(x,r)}{T_\infty}\right)^{2m}(1-\lambda), \tag{37}$$

$$u(x,r) = -\frac{\rho_\infty u_\infty}{\rho}\frac{1}{r}\frac{\partial(rg(x,r))}{\partial r}, \tag{38}$$

$$v(x,r) = \frac{\rho_\infty u_\infty}{\rho}\frac{\partial g(x,r)}{\partial x}, \tag{39}$$

where

$$g(x,r) = -\frac{r}{2}\left\{\lambda\left[1 + \frac{A}{2}\left(-\sin\left(\frac{2\pi}{L}x\right) + \cos\left(\frac{2\pi}{L}r\right)\right)\right] + (1-\lambda)\sin\left(\frac{2\pi}{L}\left[\frac{\varrho(x,y) - \varrho_i}{\varrho_f - \varrho_i}\right]^2\right)\right\} \tag{40}$$

and

$$\varrho(x,r) = \sqrt{\left(\frac{x}{a_x}\right)^2 + \left(\frac{r}{a_r}\right)^2}. \tag{41}$$

The gas pressure p is given by the state equation Eq. (8).

The parameters appearing in Eqs. (33)–(41) are presented in Table 2, except m and λ, which are used for selecting the solutions. By choosing $(m, \lambda) = (0, 1)$, $(m, \lambda) = (0, 0)$ or $(m, \lambda) = (1, 0)$, the manufactured solution for the Euler, NS-C or NS-V models can be provided, respectively.

Observe that Table 2 presents a value of ρ_∞ for Euler model ($\lambda = 1$) and another one for Navier–Stokes model ($\lambda = 0$). The last one was chosen in such a way that the Reynolds by length ($\rho_\infty u_\infty / \mu_\infty$) is 10 m^{-1}. As pointed by Roy [23], "when verifying a Navier–Stokes code, the manufactured solution should be chosen to give Reynolds numbers near unity so that convective and diffusive terms are of the same order of magnitude."

Replacing the manufactured solutions (33)–(39) into Eq. (9) results in source terms for $\phi \in \{u, v, T\}$, which were obtained with the open source symbolic manipulation software Maxima [24]. The same applies to the boundary conditions. By inserting the manufactured solutions into Eq. (25) with $r_b = 0.5$ m and $\eta = 0$, it is possible to obtain the analytical values of C_{Df} for the Euler, NS-C and NS-V models, that is, -0.0193692004363766, 0.0935033798783678 and 0.0961133712787234, respectively.

2.2.2. Solution verification

The numerical errors resulting from the solution of the partial differential equations of Section 2.1 are those generally found in Computational Fluid Dynamics [23]: round-off errors, iteration errors and discretization errors.

Round-off errors are caused by the limited representation of real numbers. Their influence on the solution may be estimated, for instance, by comparing the solution obtained with double precision floating point representation (16 significant figures) with the solution obtained with quadruple precision floating point representation (32 significant figures). In this comparison, it is assumed that the round-off error in the quadruple precision solution is vanishingly small compared to that of double precision.

Iteration error is, by definition, the difference between the numerical solution at some iteration and the exact numerical solution of the discretized model. In this work, the iterations are performed until the machine error is reached, so that the iteration errors may be considered negligibly small.

Finally, the discretization error results from approximations to the mathematical model which expresses the solution in terms of a finite number of discrete values, such as finite differences or numerical quadrature. This is typically the greatest source of the numerical error.

Considering that the round-off and iteration errors are small compared to the discretization error, in this work, the discretization error is analyzed with the convergent estimator [13] as well as with the well-known Grid Convergence Index (GCI)[7]. While GCI will provide the numerical uncertainty of the numerical solution in the finest grid, convergent estimator will provide an extrapolated solution (with an error bound), which gives a second order accurate solution from the first order numerical solution.

In order to perform the calculations, consider that three numerical solutions, ϕ_1, ϕ_2 and ϕ_3 were obtained in grids with uniform partitions h_1, h_2 and h_3, respectively, and that the grid refinement ratio r_g is a constant, *i.e.*,

$$r_g = \frac{h_2}{h_1} = \frac{h_3}{h_2} > 1. \tag{42}$$

According to the convergent estimator, the exact solution Φ of the mathematical model is bounded by the convergent estimation of the analytical solution ϕ_C and its error bound U_C, *i.e.*,

$$\phi_C - U_C \leq \Phi \leq \phi_C + U_C, \tag{43}$$

where

$$\phi_C = \frac{\phi_{\mathrm{Ri}}(p_L) + \phi_{\mathrm{Ri}}(p_U)}{2} \tag{44}$$

and

$$U_C = \frac{|\phi_{\mathrm{Ri}}(p_L) - \phi_{\mathrm{Ri}}(p_U)|}{2}. \tag{45}$$

In Eqs. (44) and (45), ϕ_{Ri} is the Richardson extrapolation of the numerical solutions based on the asymptotic order of accuracy p_L or based on the observed order of accuracy p_U. The asymptotic order of accuracy p_L is the dominant order of accuracy obtained from the truncation error for a sufficiently refined grid (first order accurate in this study, *i.e.*, $p_L = 1$) and the observed order p_U is determined by

$$p_U = \frac{\log\left(\frac{\phi_2 - \phi_3}{\phi_1 - \phi_2}\right)}{\log r_g}. \tag{46}$$

The Richardson extrapolation for an arbitrary order of accuracy p_A, and based on the finest grid h_1, is given by

$$\phi_{\mathrm{Ri}}(p_A) = \phi_1 + \frac{\phi_1 - \phi_2}{r_g^{p_A} - 1}. \tag{47}$$

The application of this estimator requires that the observed order p_U is within the convergent range, *i.e.*, that p_U decreases or increases monotonically towards p_L as the grid is refined.

According to the Grid Convergence Index, the numerical uncertainty U_{GCI} of ϕ_1 is given by

$$U_{\mathrm{GCI}} = F_s \left| \frac{\phi_1 - \phi_2}{r_g^{p_U} - 1} \right|, \tag{48}$$

where F_s is 1.25 when p_U converges to p_L in a refinement study with at least three grids, which is the case for this work. For this estimator, no extrapolation will be used and the final solution is expressed as

$$\phi_1 \pm U_{\mathrm{GCI}}. \tag{49}$$

2.3. Validation

According to the ASME V&V 20–2009 Standard [12], the modeling error δ^{model} in a simulation result ϕ^{num}, due to modeling assumptions and approximations, is expected to be within the interval

$$\mathcal{E} - U^{\mathrm{val}} \leq \delta^{\mathrm{model}} \leq \mathcal{E} + U^{\mathrm{val}}, \tag{50}$$

where $\mathcal{E}$ and U^{val} are the validation metrics. $\mathcal{E}$ is given by

$$\mathcal{E} = \phi^{\mathrm{num}} - \phi^{\mathrm{exp}} \tag{51}$$

and U^{val} depends on how the experimental result ϕ^{exp} was obtained. For the case in which ϕ^{exp} is directly measured, U^{val} reads

$$U^{\mathrm{val}} = \sqrt{(U^{\mathrm{num}})^2 + \left(U^{\mathrm{input}}\right)^2 + (U^{\mathrm{exp}})^2}, \tag{52}$$

where U^{num} is the estimate of the standard numerical uncertainty, U^{input} is the estimate of the standard uncertainty in the numerical solution caused by the variability of the input parameters and U^{exp} is the estimate of the standard uncertainty in the experimental measurement.

Since U_{GCI} empirically provides a numerical uncertainty with 95% confidence, U^{num} and U_{GCI} are related by

$$U^{\mathrm{num}} = U_{\mathrm{GCI}}/k, \tag{53}$$

where the factor k depends on the error distribution. Assuming a Gaussian distribution, ASME V&V 20–2009 Standard recommends a factor $k = 1.1$ to 1.15. In this work, it is adopted $k = 1.1$.

Considering the existence of n input parameters Z_i ($1 \leq i \leq n$), U^{input} is calculated as

$$\left(U^{\mathrm{input}}\right)^2 = \sum_1^n \left(\frac{\partial \phi^{\mathrm{num}}}{\partial Z_i} U_{Z_i} \right)^2, \tag{54}$$

where U_{Z_i} is the standard uncertainty in Z_i.

In this work, ϕ^{exp} represents the foredrag coefficient C_{Df} from the experiment of Eggers et al. [9]. The foredrag coefficient was not directly measured, but obtained from a data reduction involving some data that are input parameters for the mathematical model. Because of that, Eq. (52) is not the appropriate expression to U^{val}. The appropriate expression, however, involves experimental data that are not available. So, in this case, Eq. (52) will be used at least as an approximation to U^{val}.

3. Results and discussion

3.1. Code verification

The modified transport equations and corresponding boundary conditions resulting from the application of the Method of Manufactured Solutions, described in Section 2.2.1, were numerically solved for seven grids with $N \times N$ volumes, where N varied from 16 to 1024. Table 3 presents the error E of C_{Df} and the order of convergence p_E for the three models studied here. It is possible to observe that the error is reduced as the grid is refined and the order of convergence tends to the asymptotic order p_L, *i.e.*, $p_E \to p_L = 1$.

3.2. Solution verification

This section deals with the verification of the foredrag coefficient C_{Df} of Euler, Navier–Stokes with constant thermophysical properties (NS-C) and Navier–Stokes with variable thermophysical properties (NS-V) models in the supersonic and hypersonic regimes. Table 4 shows the free-stream Mach numbers, their corresponding free-stream Reynolds number and free-stream pressure. Table 5 presents the parameters common to all Mach number studied.

Simulations were carried out for two sets of grids. For both of them, the coarser grids were obtained from the finer one by removing every other grid line. Initially, a set with five grids m_1, m_2, m_3, m_4 and m_5 with, respectively, 60, 120, 240, 480 and 960 volumes in each coordinate direction was applied to investigate the round-off error, the iteration error, the

Table 3
C_{Df} error and the order of convergence p_E.

	Euler		NS-C		NS-V	
N	E	p_E	E	p_E	E	p_E
16	0.00685774		−0.24443152		−0.18290376	
32	0.00286248	1.26	−0.08526885	1.52	−0.06573812	1.48
64	0.00128123	1.16	−0.03192256	1.42	−0.02402013	1.45
128	0.00059186	1.11	−0.01274224	1.32	−0.00912627	1.40
256	0.00028161	1.07	−0.00532113	1.26	−0.00359801	1.34
512	0.00013691	1.04	−0.00230944	1.20	−0.00147487	1.29
1024	0.00006744	1.02	−0.00103807	1.15	−0.00062985	1.23

Table 4
Free-stream Mach number, Reynolds number and pressure.

M_∞	Re_∞	p_∞(Pa)
2.73	2.10×10^6	4.64630687×10^4
3.50	2.85×10^6	4.91844771×10^4
4.00	2.16×10^6	3.26170743×10^4
5.05	1.05×10^6	1.25588295×10^4
6.28	4.50×10^5	4.32816803×10^3

Table 5
Input parameters for the simulations.

Quantity	Symbol	Value
Length of the elliptical x semi-axis	l_a	0.08382 m
Length of the elliptical r semi-axis	l_b	0.0508 m
Base radius	r_b	0.0127 m
Fineness ratio	f	3
Parameter for grid clustering near cone tip	α	1.5
Parameter for grid clustering near cone surface	c_{bl}	0.04
Free-stream temperature	T_∞	300 K
Free-stream specific heat ratio	γ_∞	1.4000666049749
Free-stream Prandtl number	Pr_∞	$7.2449781781596 \times 10^{-1}$
Gas constant	R_g	$2.8700669426733 \times 10^2$ J kg^{-1} K^{-1}
Free-stream specific heat c_p	$(c_p)_\infty$	$1.0044039743660 \times 10^3$ J kg^{-1} K^{-1}
Free-stream viscosity	μ_∞	$1.8559826909460 \times 10^{-5}$ Pa s
Free-stream thermal conductivity	κ_∞	$2.5730324444046 \times 10^{-2}$ W m^{-1} K^{-1}

effect of grid clustering, the estimated discretization error, the effect of free-stream temperature on C_{Df} and the effect of input parameters on C_{Df}. After all these investigations had been performed, another set of simulations was carried out in an attempt to reduce still more the discretization error. This time, six grids $m'_1, m'_2, m'_3, m'_4, m'_5$ and m'_6 with, respectively, 60, 120, 240, 480, 960 and 1920 volumes in each coordinate direction were applied. Note that the grids m_1 to m_5 differ from m'_1 to m'_5, because later grids were generated from m'_6. Only the discretization error and the iteration error were reinvestigated for the set of grids m'_1 to m'_6, because the calculations in the m'_6 grid are too computationally expensive.

All simulations were performed in computers with processors Intel®Core™i5-2310 of 2.90 GHz, with 6 or 8 GB of RAM memory, where they took 8 s to 8.7 days to run and consumed 20 MB to 3.4 GB of RAM memory.

The round-off error and the iteration error were investigated in the following way. In order to evaluate the effect of the round-off error, C_{Df} was calculated using double and quadruple precision. This test was limited to a specific simulation (grid m_4 of 480 × 480 volumes and $M_\infty = 4.00$) due to the computational expense of the quadruple precision simulation. Fig. 2 shows the relative difference of C_{Df} of the Euler model, calculated with double $(C_{Df})_{dble}$ and quadruple precision $(C_{Df})_{quad}$, as a function of the number of iterations. It is possible to note that this relative difference reaches 10^{-8} during the false transient, but becomes lower than 10^{-14} for the converged solution. The same behavior occurred for the NS-C and NS-V models. The iteration error was evaluated by observing the convergence of the residuals of the linear systems and the residual of the mass conservation equation as a function of the number of iterations. Fig. 2 shows these residuals for Euler model (grid m_4 of 480 × 480 volumes and $M_\infty = 4.00$). The residual of the linear systems reaches the machine zero at about 3000 iterations, but the iteration procedure is kept until about 6000 iterations in order to ensure that the iteration errors are vanishingly small. This procedure was applied in all the simulations for all models studied here. Based on these results, we believe that both the iterative error and the round-off error are negligibly small compared to the discretization error, which allows to proceed with the calculation of the discretization error following the methodology described in Section 2.2.2. In order to estimate the discretization error, the numerical values of C_{Df} were obtained in the grids m'_1 to m'_6 (see Table 6).

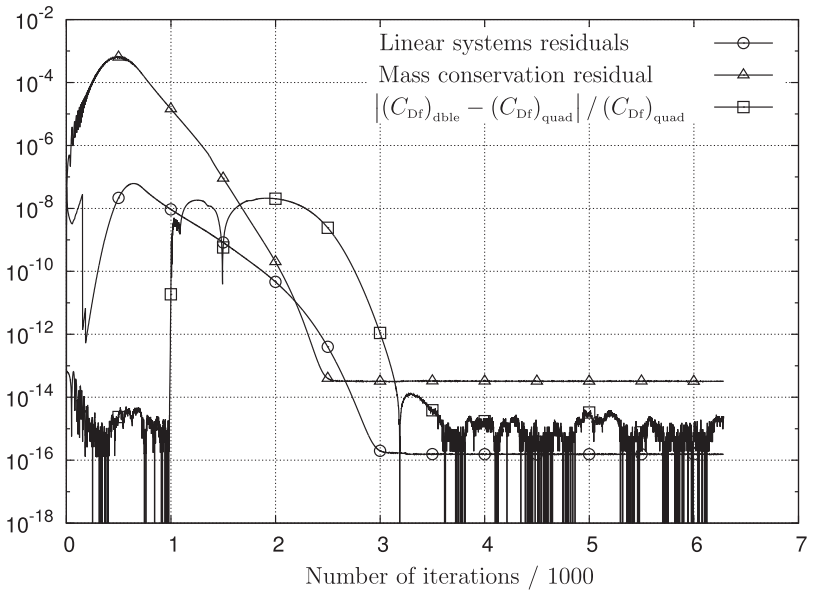

Fig. 2. Residual of the linear systems, residual of the mass conservation equation and relative difference of C_{Df} for double and quadruple precision. Euler model. Grid m_4 (480 × 480). $M_\infty = 4.00$.

Table 6
Foredrag coefficient C_{Df} numerically calculated for grids m_1' to m_6'.

	C_{Df} - Euler				
Grid	$M_\infty = 2.73$	3.50	4.00	5.05	6.28
m_1'	0.082416940	0.074810574	0.071467831	0.066729502	0.063370058
m_2'	0.082582621	0.075057714	0.071771565	0.067128413	0.063848596
m_3'	0.082700352	0.075228552	0.071975525	0.067381472	0.064136155
m_4'	0.082775126	0.075336585	0.072101505	0.067529038	0.064295830
m_5'	0.082820547	0.075401271	0.072174731	0.067610084	0.064380381
m_6'	0.082847363	0.075438176	0.072215168	0.067652831	0.064423956
	C_{Df} - NS-C				
m_1'	0.088758826	0.080001863	0.077294884	0.074799558	0.075448650
m_2'	0.088531228	0.079960190	0.077285553	0.074777812	0.075306200
m_3'	0.088574698	0.080091492	0.077458689	0.075020853	0.075598293
m_4'	0.088621125	0.080184709	0.077573375	0.075165998	0.075761940
m_5'	0.088654769	0.080243413	0.077642263	0.075246996	0.075850104
m_6'	0.088676395	0.080277755	0.077680931	0.075290090	0.075895925
	C_{Df} - NS-V				
m_1'	0.090191601	0.081672987	0.079546328	0.079185861	0.084289022
m_2'	0.090036312	0.081742923	0.079702930	0.079392142	0.084472374
m_3'	0.090105206	0.081902102	0.079911048	0.079676133	0.084816391
m_4'	0.090160145	0.082004518	0.080037664	0.079835579	0.084987265
m_5'	0.090196673	0.082066626	0.080111168	0.079922487	0.085076341
m_6'	0.090219575	0.082102540	0.080151971	0.079968176	0.085121855

Based on these results, the observed order of accuracy p_U was calculated from Eq. (46) and is shown in Table 7. The symbol — means that it was not possible to calculate p_U, because the argument of the logarithm in the numerator of Eq. (46) is non-positive, or means that p_U itself is negative. In the latter case, p_U cannot be employed, because Richardson's extrapolation diverges [13].

Once p_U was calculated, the Grid Convergence Index (GCI) and convergent estimator (CE) were applied (based on grids m_4' to m_6') to calculate, respectively, the numerical uncertainty and the extrapolated numerical solution and its error bound, which are shown in Table 8 for the three models. The values in the parenthesis represent the numerical uncertainty or the error bound, depending whether GCI or CE is applied, respectively. For instance, 0.082880(6) means 0.082880 ± 0.000006. For the whole interval of Mach numbers considered, the numerical uncertainty calculated with GCI does not exceed 0.09% of the numerical solution in the finest grid and the error bound of the convergent estimator does not exceed 0.01% of the extrapolated solution. It must be emphasized that, although the numerical scheme applied to solve the transport equations

Table 7
Observed order of accuracy p_U of the calculated foredrag coefficient C_{Df} for grids m'_1 to m'_6.

Grids\M_∞	p_U - Euler				
	2.73	3.50	4.00	5.05	6.28
(m'_1, m'_2, m'_3)	0.49	0.53	0.57	0.66	0.73
(m'_2, m'_3, m'_4)	0.65	0.66	0.70	0.78	0.85
(m'_3, m'_4, m'_5)	0.72	0.74	0.78	0.86	0.92
(m'_4, m'_5, m'_6)	0.76	0.81	0.86	0.92	0.96
	p_U - NS-C				
(m'_1, m'_2, m'_3)	–	–	–	–	–
(m'_2, m'_3, m'_4)	–	0.49	0.59	0.74	0.84
(m'_3, m'_4, m'_5)	0.46	0.67	0.74	0.84	0.89
(m'_4, m'_5, m'_6)	0.64	0.77	0.83	0.91	0.94
	p_U - NS-V				
(m'_1, m'_2, m'_3)	–	–	–	–	–
(m'_2, m'_3, m'_4)	0.33	0.64	0.72	0.83	1.01
(m'_3, m'_4, m'_5)	0.59	0.72	0.78	0.88	0.94
(m'_4, m'_5, m'_6)	0.67	0.79	0.85	0.93	0.97

Table 8
Foredrag coefficient C_{Df} obtained with the Taylor-Maccoll equation and the Euler, NS-C and NS-V models (based on the convergent estimator (CE) and based on GCI using grids m'_4 to m'_6).

	C_{Df}						
		Euler		NS-C		NS-V	
M_∞	Taylor-Maccoll	CE	GCI	CE	GCI	CE	GCI
2.73	0.082880590432055	0.082880(6)	0.08285(5)	0.088707(9)	0.08868(5)	0.090250(8)	0.09022(5)
3.50	0.075479996996251	0.075481(6)	0.07544(6)	0.080319(7)	0.08028(6)	0.082145(7)	0.08210(6)
4.00	0.072259094418355	0.072260(5)	0.07222(6)	0.077725(5)	0.07768(6)	0.080198(5)	0.08015(6)
5.05	0.067697273968818	0.067698(2)	0.06765(6)	0.075336(3)	0.07529(6)	0.080016(2)	0.07997(6)
6.28	0.064468455268321	0.064469(1)	0.06442(6)	0.075944(2)	0.07590(6)	0.085168(1)	0.08512(6)

is of first order of accuracy, the extrapolated foredrag calculated with the convergent estimator and presented in Table 8 is, at least, second order accurate, thanks to the extrapolation methodology[13].

Comparing the extrapolated C_{Df} of the Euler model (Table 8), obtained with the convergent estimator, with the solution of the Taylor-Maccoll equation [11], it was found a relative difference of less than 0.002%. The relative differences were bounded by the error bound of the convergent estimator. The Taylor-Maccoll equation is a specialization of the Euler equations obtained with the following assumptions[8]: (i) the cone is semi-infinite, (ii) the shock wave is conical and attached to the cone vertex and (iii) the flow is irrotational between the cone and the shock wave. Table 8 presents the foredrag coefficient of the Taylor-Maccoll equation calculated here based on a methodology similar to that of Sims [25]. In the present work, the Taylor-Maccoll equation was solved using quadruple precision and a fourth order Runge-Kutta method in such a way that the solution presented in Table 8 is accurate to all presented figures.

Finally, it is pointed out how the application of the convergent estimator may reduce the computational effort to obtain a solution with a given precision. Consider the numerical solution of the Euler equation at $M_\infty = 2.73$ obtained in the grid m'_6 (1920 × 1920 volumes) (Table 6), for which the relative error is 0.04% compared to the Taylor-Maccoll solution, and the extrapolated solution of the Euler equation obtained with the convergent estimator for the same condition (Table 8), for which the relative error compared to the Taylor-Maccoll solution is 0.0006%. If numerical simulations were performed in finer grids, obtained by doubling the number of volumes in each coordinate direction, and supposing that the error of the grid m'_6 is divided by two every time the grid is refined (this is the expected behavior for a first order scheme), it will be necessary, at least, a grid with 122880 × 122880 volumes in order to obtain the same precision!

3.3. Validation

Validation was performed comparing the foredrag coefficient obtained from the Euler, NS-C and NS-V models and the experimental data of Eggers et al. [9]. In this section, the numerical solution of the finest grid was not extrapolated and only GCI was applied for the quantification of its numerical uncertainty, as recommended by the ASME V&V 20–2009 Standard.

The experiment of Eggers et al. was conducted in the Ames 10- by 14-inch supersonic wind tunnel. The cone models had base diameter of 1 inch and length of 3 inches. The foredrag force was found by subtracting the base force from the total drag force, which was measured with a strain-gage balance. The forces on the base of the models were determined from measured base pressures and from free-stream static pressures. According to this research, the accuracy of the foredrag coefficients was affected by uncertainties in the measurements of the following quantities: stagnation pressures, free-stream

static pressures, base pressures, and the forces on the cone models as measured by the strain-gage balance. The combined effects of all the sources of error result in probable uncertainties in measured foredrag coefficients that varies from ± 0.001 at the low Mach numbers (2.73) to ± 0.005 at the higher Mach numbers (6.28). Since this experiment was not designed for validation, some information is not available. For instance, the uncertainty over the stagnation pressure p_0, free-stream static pressure p_∞ and dynamic pressure q_∞ are, respectively, 0.5%, 1.5% and 1.5%, but the values of these quantities were not given. On the other hand, the free-stream Mach and Reynolds numbers were given (see Table 4), but their uncertainties were not. Additionally, neither the free-stream temperature nor the base pressure (and their uncertainties) were given.

Table 9 presents the experimental foredrag coefficient C_{Df}^{exp} of Eggers et al. and its experimental standard uncertainty U^{exp}. It is relevant to mention that all the values of M_∞ read from the plot are in agreement with their nominal values given by Eggers et al., except 6.28 that was read as 6.13(2). The experimental uncertainty for $M_\infty = 2.73$ and 6.28 was given by Eggers et al. and the intermediate values were obtained by a linear interpolation. Since the data were obtained from a plot, C_{Df}^{exp} is the average value of several readings. The standard uncertainty associated with the data reading U^{read} was calculated as one standard deviation from the mean value and it is also included in Table 9. In this work, the reading standard uncertainty was combined to the experimental one to produce the total experimental standard uncertainty $U^{exp,\,t}$, *i.e.*,

$$U^{exp,t} = \sqrt{(U^{exp})^2 + (U^{read})^2}. \tag{55}$$

This additional uncertainty, that is, the reading uncertainty, is a problem often found when comparing numerical to experimental data. That is why tabulated experimental data is more suitable for validations.

After finding the estimated numerical error (see Table 8) and the experimental standard uncertainty (see Table 9), the next step should be to calculate the input uncertainty in order to estimate the validation metrics. The main input parameters are the fineness ratio f, the free-stream temperature T_∞, the free-stream Mach number M_∞ and the free-stream Reynolds number Re_∞. A couple of assumptions must be made about these parameters in order to estimate the input uncertainty, because some of them, or their standard uncertainties, are not known, as previously stated.

The uncertainty of the fineness ratio f was probably caused by direct measurements of the cone length and base diameter. Considering that a common caliper of 0.01 mm of uncertainty was applied in the measurement, the fineness ratio is affected by a relative uncertainty of 0.0017%.

Both the uncertainty of T_∞ and its value are unknown. Therefore, to evaluate how T_∞ can affect the foredrag coefficient, f, M_∞ and Re_∞ were fixed and four values of T_∞ were assumed: 200 K, 250 K, 300 K and 350 K. Table 10 shows the numerically calculated foredrag coefficient obtained on grid m_5 and its numerical uncertainty, based on grids m_3 to m_5, as a

Table 9
Experimental foredrag coefficient C_{Df}^{exp} of Eggers et al.[9], its experimental standard uncertainty U^{exp}, reading standard uncertainty U^{read} and total experimental standard uncertainty $U^{exp,\,t}$.

M_∞	C_{Df}^{exp}	U^{exp}	U^{read}	$U^{exp,\,t}$
2.73	0.0884	0.0010	0.0014	0.0017
3.50	0.0807	0.0019	0.0014	0.0024
4.00	0.0784	0.0024	0.0014	0.0028
5.05	0.0757	0.0036	0.0014	0.0039
6.28	0.0892	0.0050	0.0014	0.0052

Table 10
Effect of the free-stream temperature T_∞ on the foredrag coefficient C_{Df}.

	C_{Df} - Euler				
T_∞ (K)	$M_\infty = 2.73$	3.5	4	5.05	6.28
200	0.08282(9)	0.0754(1)	0.0722(1)	0.0676(1)	0.0644(1)
250	0.08282(9)	0.0754(1)	0.0722(1)	0.0676(1)	0.0644(1)
300	0.08282(9)	0.0754(1)	0.0722(1)	0.0676(1)	0.0644(1)
350	0.08282(9)	0.0754(1)	0.0722(1)	0.0676(1)	0.0644(1)
	C_{Df} - NS-C				
200	0.08864(9)	0.0802(1)	0.0776(1)	0.0752(1)	0.0758(1)
250	0.08865(9)	0.0802(1)	0.0776(1)	0.0752(1)	0.0758(1)
300	0.08865(9)	0.0802(1)	0.0776(1)	0.0752(1)	0.0758(1)
350	0.08865(9)	0.0802(1)	0.0776(1)	0.0752(1)	0.0759(1)
	C_{Df} - NS-V				
200	0.09037(9)	0.0823(1)	0.0804(1)	0.0804(1)	0.0859(1)
250	0.09026(9)	0.0821(1)	0.0802(1)	0.0801(1)	0.0854(1)
300	0.09019(9)	0.0821(1)	0.0801(1)	0.0799(1)	0.0851(1)
350	0.09013(9)	0.0820(1)	0.0800(1)	0.0798(1)	0.0848(1)

function of T_∞. Thus, within the numerical uncertainty, T_∞ does not affect the foredrag coefficient C_{Df} of the Euler and NS-C models, but it affects the foredrag coefficient C_{Df} of the NS-V model by an amount of up to 1.2%. Considering such result, T_∞ was fixed in 300 K with an uncertainty of 50 K.

The uncertainty of M_∞ and Re_∞ were estimated as follows. Expressing the Mach number and the Reynolds number as functions of the free-stream static pressure p_∞ and dynamic pressure q_∞, one can show that, for a fixed f and T_∞,

$$\frac{dM_\infty}{M_\infty} = \frac{1}{2}\left(\frac{dq_\infty}{q_\infty} - \frac{dp_\infty}{p_\infty}\right) \tag{56}$$

and

$$\frac{d\mathrm{Re}_\infty}{\mathrm{Re}_\infty} = \frac{1}{2}\left(\frac{dq_\infty}{q_\infty} + \frac{dp_\infty}{p_\infty}\right), \tag{57}$$

that is, the relative change of M_∞ and Re_∞ is directly proportional to relative changes in p_∞ and q_∞. Since there is a relative standard uncertainty of 1.5% over p_∞ and q_∞, we assume that the same uncertainty affects M_∞ and Re_∞.

The effect of the uncertainty of the input parameters f, T_∞, Re_∞ and M_∞ over C_{Df}, *i.e.* U^{input}, was determined based on Eq. (54). The derivatives were numerically approximated with a central differencing scheme. Table 11 shows the effect of each input parameter on C_{Df} and the estimated U^{input}. ΔC_{Df} represents the term inside the parenthesis in the right hand side of Eq. (54). The number of decimal places in this table corresponds to the accuracy of the numerical uncertainty obtained with the Grid Convergence Index based on grids m_3 to m_5. It is possible to note that the uncertainty in the free-stream Mach number is the main source of uncertainty over C_{Df}. This picture only changes for NS-V in the hypersonic regime, for which the uncertainty of both T_∞ and Re_∞ plays an important role.

Now, experimental data and numerical solutions can be compared through the validation metrics. In order to simplify the discussion and without loss of generality, it is convenient to introduce the relative validation metrics $\varepsilon = \mathcal{E}/C_{Df}^{\mathrm{exp}}$ and $\upsilon = U^{\mathrm{val}}/C_{Df}^{\mathrm{exp}}$ of C_{Df}. Table 12 presents ε and υ for the three models studied here. This table shows that the relative standard uncertainty υ did not depend on the models studied and increased with the Mach number, reaching the expressive 5.8% at $M_\infty = 6.28$. These large values of υ and their independence on the models occurred because the total experimental

Table 11
Effect of the uncertainty of the input parameters f, T_∞, Re_∞ and M_∞ on the foredrag coefficient C_{Df}.

	Euler				
M_∞	$\Delta C_{Df}(\Delta f)$	$\Delta C_{Df}(\Delta T_\infty)$	$\Delta C_{Df}(\Delta \mathrm{Re}_\infty)$	$\Delta C_{Df}(\Delta M_\infty)$	U^{input}
2.73	0.00000	0.00000	0.00000	−0.00051	0.00051
3.50	0.0000	0.0000	0.0000	−0.0004	0.0004
4.00	0.0000	0.0000	0.0000	−0.0003	0.0003
5.05	0.0000	0.0000	0.0000	−0.0003	0.0003
6.28	0.0000	0.0000	0.0000	−0.0002	0.0002
	NS-C				
2.73	0.00000	0.00000	−0.00004	−0.00052	0.00052
3.50	0.0000	0.0000	0.0000	−0.0004	0.0004
4.00	0.0000	0.0000	0.0000	−0.0003	0.0003
5.05	0.0000	0.0000	−0.0001	−0.0003	0.0003
6.28	0.0000	0.0000	−0.0001	−0.0002	0.0002
	NS-V				
2.73	0.00000	−0.00006	−0.00006	−0.00049	0.00050
3.50	0.0000	−0.0001	−0.0001	−0.0004	0.0004
4.00	0.0000	−0.0001	−0.0001	−0.0003	0.0003
5.05	0.0000	−0.0002	−0.0001	−0.0002	0.0003
6.28	0.0000	−0.0003	−0.0002	−0.0001	0.0003

Table 12
Relative validation metrics ε and υ.

	Euler		NS-C		NS-V	
M_∞	ε (%)	υ (%)	ε (%)	υ (%)	ε (%)	υ (%)
2.73	−6.3	2.0	0.3	2.0	2.0	2.0
3.50	−6.6	3.0	−0.6	3.0	1.7	3.0
4.00	−7.9	3.6	−0.9	3.6	2.2	3.6
5.05	−11	5.1	−0.5	5.1	5.7	5.1
6.28	−28	5.8	−15	5.8	−4.6	5.8

standard uncertainty $U^{\text{exp, t}}$ was the main source of error and dominated over the input U^{input} and numerical U^{num} standard uncertainties.

In accordance to the ASME V&V 20–2009 Standard, $\mathcal{E}$ represents an estimation of the model error and U^{val} represents its standard uncertainty. The relative validation metrics ε and υ have an analogous interpretation. Conclusions on the model's accuracy depend on the ratio $|\varepsilon/\upsilon|$. The interpretation can be made simpler by plotting ε with its error bar υ. If the error bar is close to the horizontal axis in the graph ($|\varepsilon/\upsilon| \lesssim 1$), then the combined input error, experimental error and numerical error is of the same order of the model error. In this case, it is not possible to evaluate if the difference between the experimental and numerical results was caused by the model error or by the other source of errors. On the other hand, if the error bar is small compared to the distance of ε to the horizontal axis ($|\varepsilon/\upsilon| \gg 1$), then probably ε is a good estimation of the model error.

Fig. 3a, c and e compare the foredrag coefficient C_{Df} from the Euler, NS-C and NS-V models, respectively, with the experimental data. These figures present only the numerical and experimental error bars (note that numerical error bars are much smaller than the experimental ones). Fig. 3b, d and f present the corresponding estimated relative model error ε of each model. Based on the interpretation of the ASME V&V 20–2009 Standard, we can note that: a) the Euler model presented the

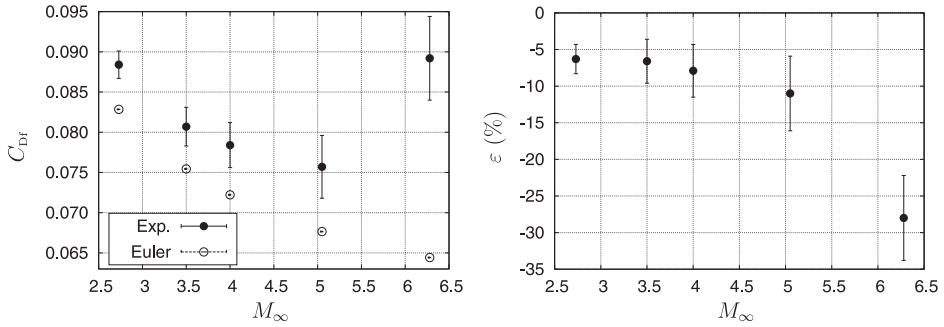

(a) Experimental *vs* Euler model

(b) Estimated relative model error for Euler

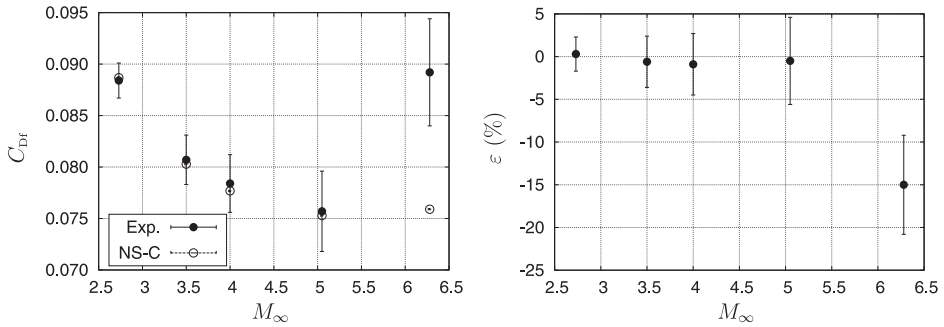

(c) Experimental *vs* NS-C model

(d) Estimated relative model error for NS-C

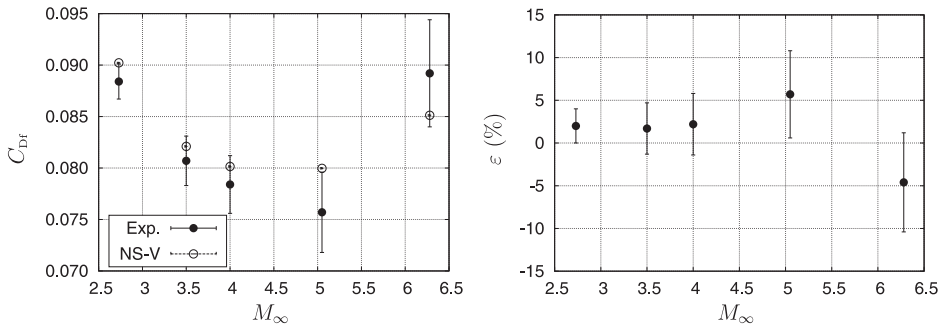

(e) Experimental *vs* NS-V model

(f) Estimated relative model error for NS-V

Fig. 3. Comparison of the numerical and experimental foredrag coefficient C_{Df}.

greatest model error for the whole set of Mach numbers studied. The relative estimated model error ε varied from −6.3% to −28%. The ratio $|\varepsilon/\upsilon|$ was always greater than 2, which indicates that ε is a good estimation of the model error; b) the Navier-Stokes with constant thermophysical properties (NS-C) improved the modeling compared to the Euler model. For $M_\infty \leq 5.05$, $|\varepsilon| \leq 0.9\%$ and $|\varepsilon/\upsilon| < 1$. But for $M_\infty = 6.28$, we found a relative estimated model error of 15% with $|\varepsilon/\upsilon| = 2.5$; c) taking into account the validation standard uncertainty, the Navier-Stokes model with variable thermophysical properties (NS-V) agreed better with the experimental data over the whole interval of M_∞ studied. The maximum relative estimated model error was 5.7% with $|\varepsilon/\upsilon| \leq 1.1$.

Fig. 3a, c and e compare the foredrag coefficients of the Euler, NS-C and NS-V models as a function of the free-stream Mach number. It is important to mention that the free-stream Reynolds number is not constant in these figures, but changes with M_∞, as shown in Table 4. According to the Euler model (inviscid flow), the foredrag coefficient decreases monotonically with M_∞. This does not occur in the NS-C model, because the increased flow speed associated with the decreased Reynolds number increases the viscous stress over the cone surface, which, consequently, increases the foredrag coefficient. This effect is augmented in the NS-V model due to the large variations in the temperature field, which affects the thermophysical properties c_p, μ and κ and, consequently, the foredrag coefficient.

Finally, for the sake of curiosity, Fig. 4 shows some isolines of Mach number, pressure and temperature obtained from the numerical solution of the NS-V model at free-stream Mach number $M_\infty = 6.28$ in the grid m'_6. Contrary to the Euler's solution, the isolines are not straight lines, particularly near the cone tip. Although this result is shown for a particular case, it was observed for the other values of M_∞.

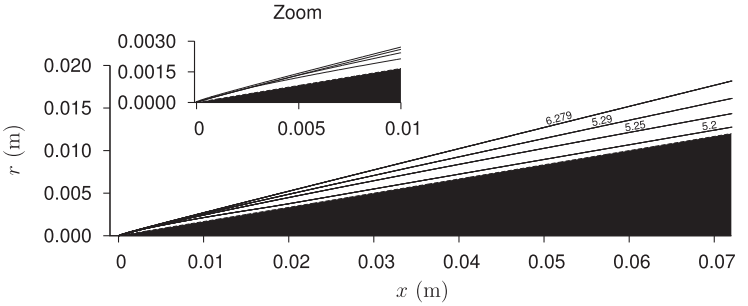

(a) Isolines of the Mach number

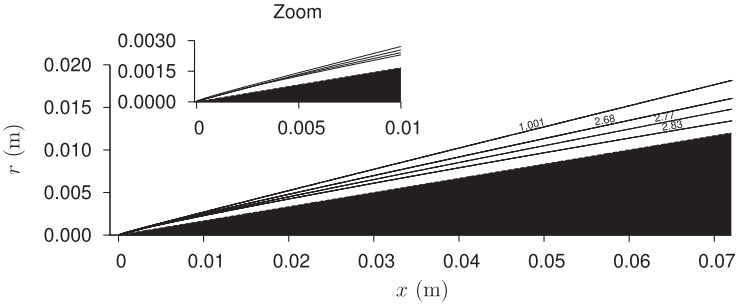

(b) Isolines of the pressure ratio p/p_∞

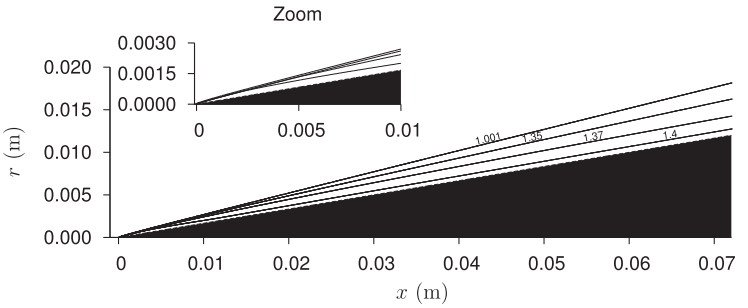

(c) Isolines of the temperature ratio T/T_∞

Fig. 4. Isolines of M, p and T for NS-V at $M_\infty = 6.28$.

4. Conclusion

The verification of the foredrag coefficient for the Euler model, the Navier-Stokes model with constant thermophysical properties and the Navier-Stokes model with variable thermophysical properties showed that the numerical error was dominated by the discretization error, *i.e.*, the iteration error and the round-off error were negligibly small.

For all the Mach numbers considered, the observed order of accuracy, calculated with five or six grids, converged to the asymptotic one, allowing one to apply the convergent estimator for evaluation of the discretization error. The error bound did not exceed 0.01% of the extrapolated solution for all models.

The relative difference between the Euler and the Taylor-Maccoll foredrag coefficients reached up to 0.002%, which was bounded by the error bound of the convergent estimator.

The validation metrics of the foredrag coefficient showed that the Navier-Stokes model with variable thermophysical properties (NS-V) agreed better with experimental data for the whole set of Mach number studied. The greatest relative difference between numerical and experimental foredrag for the NS-V model was 5.7% with a relative validation standard uncertainty of 5.1%. For the other two models, *i.e.*, Euler and Navier-Stokes with constant thermophysical properties (NS-C), the absolute value of the relative estimated model error varied from 6.3% to 28% and from 0.3% to 15%, respectively. Despite the 15% relative estimated model error of the NS-C model, that occurred for $M_\infty = 6.28$, for the remaining Mach numbers studied, comparison of the modeling error of the NS-C and the NS-V models was inconclusive, because the validation standard uncertainties were of the same order of the estimated modeling errors. The relative validation standard uncertainty varied from 2% to 5.8% for all models and was dominated by the standard uncertainty of the experimental data. Because of that, no further grid refinement study would improve the comparison of the modeling errors of the NS-C and NS-V models.

Acknowledgment

We would like to thank CNPq (National Counsel of Technological and Scientific Development, Brazil) (309365/2013-9), CAPES (Coordination for the Improvement of Higher Education Personnel, Brazil) (Project n. 20 of Edital Pró-Estratégia 50/2011), for their financial support, and UTFPR-FB (Universidade Tecnológica Federal do Paraná-Francisco Beltrão), SINAPAD (Sistema Nacional de Processamento de Alto Desempenho), particularly CESUP and CENAPAD-UFC, for their technological support. The second author is supported by a CNPq scholarship. We are also grateful for the suggestions provided by the reviewers.

References

[1] C.J. Roy, W.L. Oberkampf, A comprehensive framework for verification, validation, and uncertainty quantification in scientific computing, Comput. Methods Appl. Mech. Eng. 200 (25–28) (2011) 2131–2144, doi:10.1016/j.cma.2011.03.016.
[2] I. Babuska, J. Oden, Verification and validation in computational engineering and science: basic concepts, Comput. Methods Appl. Mech. Eng. 193 (36–38) (2004) 4057–4066, doi:10.1016/j.cma.2004.03.002.
[3] W. Oberkampf, T. Trucano, Verification and validation in computational fluid dynamics, Progr. Aerosp. Sci. 38 (3) (2002) 209–272, doi:10.1016/S0376-0421(02)00005-2.
[4] P. Roache, Quantification of uncertainty in computational fluid dynamics, Ann. Rev. Fluid Mech. 29 (1997) 123–160, doi:10.1146/annurev.fluid.29.1.123.
[5] P.J. Roache, Verification and Validation in Computational Science and Engineering, Hermosa, Albuquerque, N.M., c1998.
[6] W.L. Oberkampf, C.J. Roy, Verification and Validation in Scientific Computing, 1st ed., Cambridge University Press, New York, 2010.
[7] P.J. Roache, Fundamentals of Verification and Validation, Hermosa Publishers, Socorro, New Mexico, 2009.
[8] J.D. Anderson Jr., Modern Compressible Flow: With Historical Perspective, 3rd ed., McGraw-Hill, New York, 2003.
[9] A.J. Eggers Jr., M.M. Resnikoff, D.H. Dennis, Bodies of Revolution Having Minimum Drag at Hypersonic Airspeeds, Report 1306, NACA, 1956.
[10] G. Bertoldo, C.H. Marchi, L.K. Araki, D.F. Moro, E.M. Germer, J.J. Radtke, Verificação e validação do coeficiente de arrasto frontal para escoamento supersônico e hipersônico de ar sobre cones, in: II Congresso de Matemática Aplicada e Computacional - SUDESTE (CMAC-SE), 2013, pp. 88–92.
[11] G.I. Taylor, J.W. Maccoll, The air pressure on a cone moving at high speeds, in: Proceedings of the Royal Society of London. Series A, Containing Papers of a Mathematical and Physical Character, 139, 1933, pp. 278–297. (838)
[12] ASME, Standard for Verification and Validation in Computational Fluid Dynamics and Heat Transfer, ASME V&V 20–2009, 2009.
[13] C.H. Marchi, A.F.C. Silva, Unidimensional numerical solution error estimation for convergent apparent order, Numer. Heat Transf. Part B Fundam. 42 (2) (2002) 167–188, doi:10.1080/10407790190053888.
[14] C.H. Marchi, A.F.C. Silva, Multi-dimensional discretization error estimation for convergent apparent order, J. Braz. Soc. Mech. Scie. Eng. 27 (4) (2005) 432–439, doi:10.1590/S1678-58782005000400012.
[15] R.B. Bird, W.E. Stewart, E.N. Lightfoot, Transport Phenomena, 2nd ed., John Wiley & Sons, 2002.
[16] B.J. McBride, S. Gordon, M.A. Reno, Coefficients for Calculating Thermodynamic and Transport Properties of Individual Species, Technical Memorandum 4513, NASA, 1993.
[17] G.P. Sutton, O. Biblarz, Rocket Propulsion Elements: An Introduction to the Engineering of Rockets, 7th ed., John Wiley & Sons, United States, 2001.
[18] C.H. Marchi, C.R. Maliska, A nonorthogonal finite-volume method for the solution of all speed flows using co-located variables, Numer. Heat Transf. 26 (3) (1994) 293–311, doi:10.1080/10407799408914931.
[19] H.K. Versteeg, W. Malalasekera, An Introduction to Computational Fluid Dynamics: the Finite Volume Method, Longman Scientific & Technical, Harlow, Essex, England, 1995.
[20] J.P. Van Doormaal, G.D. Raithby, Enhancements of the SIMPLE method for predicting incompressible fluid flows, Numer. Heat Transf. 7 (1984) 147–163, doi:10.1080/01495728408961817.
[21] J.H. Ferziger, M. Peric, Computational Methods for Fluid Dynamics, 3rd ed., Springer, 2002.
[22] G.E. Schneider, M. Zedan, A modified strongly implicit procedure for the numerical solution of field problems, Numer. Heat Transf. 4 (1981) 1–19, doi:10.1080/01495728108961775.
[23] C. Roy, Review of code and solution verification procedures for computational simulation, J. Comput. Phys. 205 (1) (2005) 131–156, doi:10.1016/j.jcp.2004.10.036.
[24] Maxima, Maxima, a Computer Algebra System. version 5.34.1, 2014. http://maxima.sourceforge.net/ last access date 26 November 2016.
[25] J.L. Sims, Tables for Supersonic Flow Around Right Circular Cones at Zero Angle of Attack, Technical Report SP-3004, NASA, 1964.